Autonomous Distributed 3D Radiation Field Estimation for Nuclear Environment Characterization

Frank Mascarich[1], Paolo De Petris[1,2], Huan Nguyen[1,2], Nikhil Khedekar[1] and Kostas Alexis[1,2]

Abstract— This paper contributes a method designed to enable autonomous distributed 3D nuclear radiation field mapping. The algorithm uses a single radiation sensor and a sequence of spatially distributed and robotically acquired radiation measurements across a discretized 3D grid to derive a radiation gradient. The derived gradient is probabilistically propagated to unknown components of the map to further guide a curiosity-driven path planner by identifying the next most radiologically informative point given available information. To demonstrate the method, we develop a resilient micro flying robot capable of autonomous GPS-denied navigation that integrates a Thallium–doped Cesium Iodide (CsI(Tl)) scintillator and Silicon Photomultiplier (SiPm) combined with custom–built pulse counting circuitry. A set of experimental studies is presented inside an indoor facility within which actual radioactive uranium ore sources have been distributed.

Fig. 1. The Resilient Micro Flyer-γ nuclear distributed radiation field characterization robot and an instance of a relevant mission.

I. INTRODUCTION

Nuclear energy continues to maintain a major role in society. Currently, about 11% of the world's electricity is produced from approximately 450 active nuclear reactors, while 50 countries make further use of 225 reactors for research, the production of medical and industrial isotopes, as well as training [1]. At the same time, $27,000$ nuclear weapons are documented in the world and thousands are deployed on land, at sea, and in the air. The above is in addition to a history of developments that have left behind tons of nuclear waste, often in less than ideal containment conditions. Therefore, radiological measurements and surveying operations, source localization, distributed field mapping and illicit source identification are tasks of paramount importance and unparalleled value within a collection of scenarios ranging from environmental contamination, monitoring of nuclear waste sites, rapid response, security operations and more. It is thus important that the technology of radiation mapping and characterization further improves.

Motivated by the facts above, in this work we contribute the full algorithm design and system realization to facilitate the autonomous estimation and mapping of distributed 3D radiation fields inside complex and possibly confined facilities. Departing from traditional source localization or estimation over strictly 2D fields, this work deals with the problem of complex field distributions as they can appear when radioactive materials are spatially distributed in the three spatial dimensions. Exploiting the structure of the
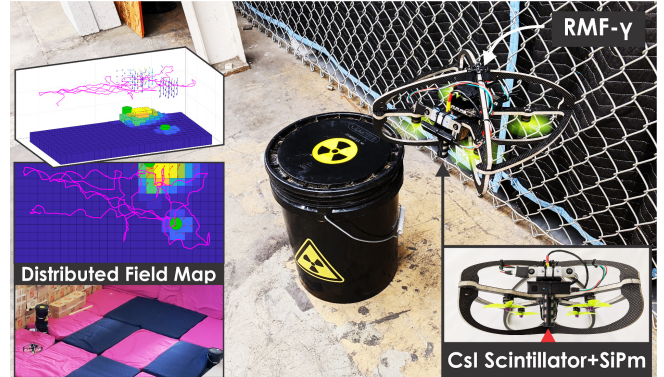
problem, this first involves the modeling of 3D radiation fields using a discretized grid and aggregating sequentially acquired measurements both to update the best estimate of the radiation intensity and to derive a radiation gradient. The derived gradient is probabilistically propagated towards unknown areas of the map in order to determine areas of maximum uncertainty and thus guide a curiosity-driven path planner such that an aerial robot integrating a scintillator can navigate to acquire the next-most-informative-measurement and thus best support the field estimation process. Given that important radiation characterization missions frequently have to take place in challenging indoor environments, our work culminates with embedding this functionality in a micro aerial vehicle with a resilient collision-tolerant design and GPS-denied navigation capabilities. The system, named the "Resilient Micro Flyer-γ" (RMF-γ) after the fact that it detects gamma radiation, integrates a Thallium-doped Cesium Iodide (CsI(Tl)) scintillator combined with a Silicon Photomultiplier (SiPm) and exploits visual-inertial odometry, alongside a 3D Time-of-Flight camera for dense mapping.

To evaluate the method, a set of experimental studies are presented. More specifically, in two missions the RMF-γ is deployed inside an indoor facility to estimate the distributed nuclear radiation field emitted by buckets of radioactive uranium ore. In the first experiment, the robot collects radiation readings guided by the curiosity-driven informative planning policy and achieves faster mapping, whereas in the second study we compare against a fixed lawnmower path. As shown, high-quality radiation maps are derived.

The remainder of this paper is organized as follows. Section II outlines related work, followed by the problem statement in Section III. The proposed method and robot design are detailed in Section IV and V. Evaluations are detailed in Section VI, followed by conclusions in Section VII.

[1] University of Nevada, Reno, 1664 N. Virginia, 89557, Reno, NV, USA `fmascarich@nevada.unr.edu`
[2] NTNU, O. S. Bragstads Plass 2D, 7034, Trondheim, Norway.

II. RELATED WORK

The area of radiation field mapping and source localization has been studied through a set of contributions such as [2–6]. Among them, maximum likelihood estimation is utilized in [4, 6], numerical adjoints in conjuction to a bayesian formulation are used in [2], while a particle filter is employed in [3]. These methods focus on the problem of estimating discrete sources and tend to assume the availability of a large number of spatially distributed measurements - typically provided using an array of fixed sensors. Focusing on the problem of distributed field estimation, existing work has emphasized non-nuclear applications via networks of wireless sensors [7, 8], while relevant robotics research exists yet remains less common [9]. Active source (e.g. radiological, chemical) localization has been studied in [10–12]. In the specific field of nuclearized robotics, a set of works [13–20] have presented interesting results. The authors in [20] propose a successive-elimination approach to adaptive source seeking. The work in [13] details a distributed guidance strategy to estimate the radiation distribution and test their method using a "radiation analog" source. The contributions in [14, 17] handle multiple sources but only evaluate their methods in simulation. Aerial robotic semantic scene segmentation is used in [15] in order to better inform the information gathering trajectories of a ground robot. The contribution in [16] uses a helicopter UAV to map radiation over large environments, while the work in [18] refers to post–disaster radiation mapping and a grid–based bayesian estimator for single source localization and contour analysis for multiple sources. Our previous works in the domain [21, 22] have focused on either single source localization or 2D only field estimation using either flying or ground systems. In comparison, this work focuses on distributed 3D radiation field estimation and simultaneous informative path planning to identify the next-best-sampling point for scintillator readings to be collected. At the same time, the work involves a resilient micro flyer design such that nuclear radiation missions can be conducted in GPS-denied and confined environments exploiting the system's collision-tolerance.

III. PROBLEM DESCRIPTION

This work considers the problem of autonomous estimation of the underlying spatial distribution of a nuclear radiation field within an initially unknown environment. This is organized into the main problem of determining the distribution and intensity of the field and the subproblem of identifying a sequence of informative points over which readings should be gathered to support the estimation task.

Problem 1 (Distributed 3D Radiation Field Mapping) Given a bounded but initially unknown 3D volume $\mathcal{V}$ and a set of measurements $\{\boldsymbol{\lambda}_m\}$, each containing the position $\mathbf{p}_m$ at which the measurement took place and a radiation measurement γ_m, the goal is to estimate the underlying spatial distribution $\mathcal{M}(\mathbf{p}_m)$ which best fits all data in $\{\boldsymbol{\lambda}_m\}$ and accurately predicts the true field distribution at every possible test location $\mathbf{p}_m$ within $\mathcal{V}$.

Problem 2 (Informative Waypoint Selection) Given this problem definition and the co-estimation of not only the mean of the nuclear radiation field intensity but also a metric of the underlying uncertainty, the second problem addressed in this work relates to iteratively identifying waypoints over which additional radiation measurements are to be acquired, then an optimized reduction in the field uncertainty is achieved and thus a best iterative map update takes place.

IV. 3D DISTRIBUTED RADIATION MAPPING

The proposed method addresses the problem of autonomous distributed 3D radiation field estimation and proposes both an algorithm to estimate the field given a set of sequentially collected measurements, and an information-sampling planner to iteratively decide the next-most-informative point for a robotic system to go in order to best support the field mapping process and thus acquire high-quality results in a rapid manner. The underlying motivational scenario is that an aerial robot will have to enter a large radioactive area and manage to derive an accurate radiation map identifying distributed nuclear intensity values across it in a fast manner and despite the hard endurance constraints of Micro Aerial Vehicles (MAVs).

Let the robot configuration at time t_k be the flat state $\boldsymbol{\xi}_k = [\mathbf{p}_k | \psi_k]$ corresponding to a position $\mathbf{p}_k = [x_k, y_k, z_k]$ and heading ψ_k. Then the system, as detailed for our robot in Section V, is considered to integrate a scintillator providing an associated radiation count reading γ_k, measured in Counts Per Second (CPS), as detailed in [21]. The proposed method is tailored to distributed radiation fields and thus the specific structure of the problem is exploited. In particular, a distributed radiation field can be thought of as the aggregated effect of a large number of point sources, each of them following the inverse square law for their intensity and a Poisson model for the noise of an associated measurement. By the aggregation of the noise terms and assuming locally smooth spatial variation of the intensity of the field, then given sufficient sampling density, the problem can be approached with multiple local regressions.

In reference to the notations listed in Table I, the proposed method discretizes a bounded volume into a 3D grid of cells where the discretization resolution, $\boldsymbol{D}_M$ is a tunable factor. Measurements are pose-annotated by the system's onboard odometry solution, and the pose-annotated measurements $\boldsymbol{\lambda}_k = [\boldsymbol{\xi}_k | y_k]$ are added to a list of readings maintained by the corresponding cell. This allows the algorithm's most critical functionality, namely gradient estimation and propagation to run at a rate independent of data collection.

The algorithm consists of three independent stages, namely a) estimation, b) propagation, and c) curiosity derivation. In the estimation stage, the set of spatially distributed readings are utilized over the discretized 3D grid to co-estimate a mean intensity and an estimated gradient, as well as the corresponding confidence metrics for each grid cell. In the propagation phase, the estimated gradient in each cell, alongside a confidence metric based on the spatial entropy of the cell's neighborhood measurements, is propagated

$\mathbb{M}$	Discretized Grid Map
$i, j, k \in \mathbb{Z}^+$	Cell indexes along the x, y, z axes
$\mathbb{C}_{ijk}$	Grid cell at index i, j, k
$\mathbf{D}_M \in \mathbb{R}^3$	Grid cell size in meters along x, y, z axes
$N_{ijk}, N_{ijk}^{nb} \in \mathbb{R}$	Number of measurements γ_m within $\mathbb{C}_{ijk}$ and $\mathbb{C}_{ijk}$'s neighborhood respectively
$\mathbf{X}_{ijk} \in \mathbb{R}^{n \times 4}$	Matrix of measurement positions within $\mathbb{C}_{ijk}$'s neighborhood, offset by the average measurement position, and appended with the column vector $\mathbf{1}$ at the end (the number of rows $n = N_{ijk}^{nb}$)
$\mathbf{S}_{ijk} \in \mathbb{R}^n$	Vector of measurements within $\mathbb{C}_{ijk}$'s neighborhood (the number of rows $n = N_{ijk}^{nb}$)
$\mu_{ijk}^m, \sigma_{ijk}^m \in \mathbb{R}$	Estimated mean, mean confidence at $\mathbb{C}_{ijk}$
$\boldsymbol{\delta}_{ijk}^m, \mathbf{H}_{ijk}^m \in \mathbb{R}^3$	Vectors of estimated gradient, gradient confidence at $\mathbb{C}_{ijk}$
$\mathbb{O}^\mu, \mathbb{O}^\delta$	Cell propagation ordering for mean and gradient over $\mathbb{M}$
$\mu_{ijk}^p, \sigma_{ijk}^p \in \mathbb{R}$	Propagated mean, mean confidence at $\mathbb{C}_{ijk}$
$\boldsymbol{\delta}_{ijk}^p, \mathbf{H}_{ijk}^p \in \mathbb{R}^3$	Vectors of propagated gradient, gradient confidence at $\mathbb{C}_{ijk}$
$L_{ijk}^\mu, L_{ijk}^\delta \in \mathbb{Z}^+$	$\mathbb{C}_{ijk}$'s Propagation *Level*s for the mean and gradient vector
$\rho_{ijk} \in \mathbb{R}$	$\mathbb{C}_{ijk}$'s Radiation Curiosity
$(\mathbf{a}^x, \mathbf{a}^y, \mathbf{a}^z)$	x, y, z components of vector $\mathbf{a} \in \mathbb{R}^3$

to unknown neighboring cells using a weighted average. The measured and propagated gradients are then used to propagate an estimated mean radiation intensity for each cell. In the final phase, a curiosity waypoint is found by combining the estimated mean radiation intensity with the spatial entropy of measurements in a cell's neighborhood in order to find the most radiation-informative point for the next iteration of the method.

A. Gradient Estimation

For a cell $\mathbb{C}_{ijk} \in \mathbb{M}$, we define $\mathbb{C}_{ijk}$'s neighbors as the cells which share edges or faces with $\mathbb{C}_{ijk}$. The gradient estimation phase only considers measurements obtained locally within a neighborhood region (including $\mathbb{C}_{ijk}$ and $\mathbb{C}_{ijk}$'s neighbors) around the cell $\mathbb{C}_{ijk}$. Iterating over each $\mathbb{C}_{ijk} \in \mathbb{M}$, the process first counts the number of readings present in $\mathbb{C}_{ijk}$ (N_{ijk}) to determine if $\mathbb{C}_{ijk}$ has sufficient readings to estimate a mean and gradient. If N_{ijk} is small (in this work less than 5), it is considered to be an unmeasured cell. If $\mathbb{C}_{ijk}$ has sufficient readings, the algorithm gathers all readings within $\mathbb{C}_{ijk}$'s neighborhood region and runs linear regression as in Eq. (1) to find the best-fit spatial gradient vector and mean:

$$\begin{bmatrix} \boldsymbol{\delta}_{ijk}^m \\ \mu_{ijk}^m \end{bmatrix} = (\mathbf{X}_{ijk}^T \mathbf{X}_{ijk})^{-1} \mathbf{X}_{ijk}^T \mathbf{S}_{ijk} \quad (1)$$

These values are assigned as the cell's measured gradient vector, $\boldsymbol{\delta}_{ijk}^m$ and measured mean μ_{ijk}^m. In the event the columns of the cell's measurement position matrix, $\mathbf{X}_{ijk}$ are not linearly independent, μ_{ijk}^m is calculated as a simple average of the N_{ijk}^{nb} readings present in the neighborhood.

However, this is a rare occurrence given the noise associated with onboard odometry estimation.

If the measured mean μ_{ijk}^m is less than a threshold defined by a small scalar multiple of the background radiation level, $\boldsymbol{\delta}_{ijk}^m$ is assigned as $[0, 0, 0]^T$ to prevent gradients with a low Signal-to-Noise Ratio (SNR) from being propagated falsely. This threshold is chosen such as to minimize the effect of poorly estimated gradients whose means are near background, while at the same time not dismissing derived gradients at the edge of a meaningful radiation field generated by actual sources.

Finally, the algorithm calculates confidence metrics for $\boldsymbol{\delta}_{ijk}^m$ and μ_{ijk}^m. The spatial entropy vector of the measurements obtained in $\mathbb{C}_{ijk}$'s neighborhood, $\mathbf{H}_{ijk}^m$, is found in order to provide a confidence metric for $\boldsymbol{\delta}_{ijk}^m$. A histogram of measurement positions projected onto each axis is constructed using b_h bins (in this work $b_h = 10$) and is bounded by the limits of the neighborhood along that axis. Shannon Entropy is then calculated on this histogram by Eq. (2):

$$\begin{aligned} \mathbf{H}_{ijk}^{m,h} &= -\sum_{w=1}^{b_h} P(h_w) \log P(h_w) \quad (2) \\ \mathbf{H}_{ijk}^m &= [\mathbf{H}_{ijk}^{m,x}, \mathbf{H}_{ijk}^{m,y}, \mathbf{H}_{ijk}^{m,z}]^T \end{aligned}$$

where h_w is the number of measurements projected along the h-axis ($h \to x, y, x$) found in bin w, and $P(h_w)$ is found by Eq. (3):

$$P(h_w) = \frac{h_w}{\sum_{i=1}^{b_h} h_i} \quad (3)$$

A metric of the estimated mean's confidence is calculated by a simple linear equation corresponding to the total number of measurements used to estimate the mean as in Eq. (4):

$$\sigma_{ijk}^m = 1 - \frac{3}{N_{ijk}^{nb}}, \quad \sigma_{ijk}^m \in [0, 1] \quad (4)$$

Algorithm 1 outlines the gradient estimation process.

Algorithm 1 Measured Gradient Estimation

1: **for** $\mathbb{C}_{ijk} \in \mathbb{M}$ **do**
2:     **if** $N_{ijk} > 4$ **then**
3:         *Find neighbors of* $\mathbb{C}_{ijk}$
4:         *Construct* $\mathbf{X}_{ijk}$ *and* $\mathbf{S}_{ijk}$
5:         **if** $det(\mathbf{X}_{ijk}^T \mathbf{X}_{ijk})! = 0$ **then**
6:             *Calculate* $\boldsymbol{\delta}_{ijk}^m, \mu_{ijk}^m$ *by Eq. (1)*
7:             *Calculate* $\mathbf{H}_{ijk}^m$ *by Eq. (2)*, (3)
8:         **else**
9:             $\mu_{ijk}^m \leftarrow Average(\mathbf{S}_{ijk})$
10:        **end if**
11:        *Calculate* σ_{ijk}^m *by Eq. (4)*
12:        **if** $\mu_{ijk}^m < background\_threshold$ **then**
13:            $\boldsymbol{\delta}_{ijk}^m \leftarrow \mathbf{0}_{1 \times 3}$
14:        **end if**
15:     **end if**
16: **end for**

B. Gradient Propagation

The process of mean and gradient propagation takes place over a carefully dictated cell ordering, starting with cells whose means and gradients have been respectfully estimated as in Algorithm 1 and continuing onto their neighbors. After the gradient estimation step, a cell has a valid mean if the condition in line 2 of Algorithm 1 is satisfied; whereas a cell has a valid gradient vector if the conditions in lines 2, 5 of Algorithm 1 are satisfied. In order to generate the propagation orders, for each cell, the method defines separate propagation *Level*s for the mean (L_{ijk}^{μ}) and gradient vector (L_{ijk}^{δ}) by a recursive method, for which the derivation of L_{ijk}^{μ} is detailed in Algorithm 2, while the derivation of L_{ijk}^{δ} follows a similar procedure. Distinct propagation orders, $\mathbb{O}^{\mu}$, $\mathbb{O}^{\delta}$, are derived for the mean propagation and gradient propagation processes based on an incremental ordering of L_{ijk}^{μ} and L_{ijk}^{δ}.

Algorithm 2 Cell Mean Level Derivation L_{ijk}^{μ}

1: $NextLayer, CurrentLayer \leftarrow \varnothing$ ▷ (Empty Set)
2: **for** $\mathbb{C}_{ijk} \in \mathbb{M}$ **do**
3:     $L_{ijk}^{\mu} \leftarrow NaN$
4:     **if** $N_{ijk} > 4$ **then**
5:        Add $\mathbb{C}_{ijk}$ to $CurrentLayer$
6:     **end if**
7: **end for**
8: $i \leftarrow 0$
9: **while** $CurrentLayer \; ! = \varnothing$ **do**
10:     **for** $\mathbb{C}_{ijk} \in CurrentLayer$ **do**
11:        $L_{ijk}^{\mu} = i$
12:        **for** $\mathbb{C}_{i'j'k'} \in Neighbors(\mathbb{C}_{ijk})$ **do**
13:           **if** $L_{i'j'k'}^{\mu} = NaN$ **then**
14:              Add $\mathbb{C}_{i'j'k'}$ to $NextLayer$
15:           **end if**
16:        **end for**
17:     **end for**
18:     $CurrentLayer \leftarrow NextLayer$
19:     $NextLayer \leftarrow \varnothing$
20:     $i \leftarrow i + 1$
21: **end while**

Once the propagation orderings are derived, the gradients are propagated first. For each cell, $\mathbb{C}_{ijk}$ in the gradient propagation ordering, $\mathbb{O}^{\delta}$, the method finds its neighbors. For cells whose $L_{ijk}^{\delta} = 0$, the cell's propagated gradient vector ($\boldsymbol{\delta}_{ijk}^{p}$) and gradient confidence vector ($\mathbf{H}_{ijk}^{p}$) are assigned to the corresponding estimated values $\boldsymbol{\delta}_{ijk}^{m}$ and $\mathbf{H}_{ijk}^{m}$ of the cell, respectively. Otherwise, the cell's $\boldsymbol{\delta}_{ijk}^{p}$ is calculated as the weighted average of its neighbors' $\boldsymbol{\delta}_{ijk}^{p}$, using only neighbors with L_{ijk}^{δ} less than that of the cell in question, and weighted by the neighbor's $\mathbf{H}_{ijk}^{p}$. The cell's $\mathbf{H}_{ijk}^{p}$ is derived as the average of the utilized neighbors' $\mathbf{H}_{ijk}^{p}$. Once gradient propagation is complete, mean propagation takes place following a similar procedure to that detailed in our previous work [22] and is presented in Algorithm 3. In particular, we iterate over cells in the mean propagation

order, $\mathbb{O}^{\mu}$. For cells whose $L_{ijk}^{\mu} = 0$, their propagated mean (μ_{ijk}^{p}) and mean confidence (σ_{ijk}^{p}) are assigned to the corresponding estimated values μ_{ijk}^{m} and σ_{ijk}^{m} of the cell, respectively. For cells of all other levels, the method finds neighbors ($\mathbb{C}_{i'j'k'}$) of the cell whose $L_{i'j'k'}^{\mu}$ is less than that of the cell in question ($\mathbb{C}_{ijk}$), and calculates their corresponding contribution following the equations:

$$\mu_{i'j'k' \rightarrow ijk}^{p} = \mu_{i'j'k'}^{p} + \begin{bmatrix} (i-i')\mathbf{D}_M^x \\ (j-j')\mathbf{D}_M^y \\ (k-k')\mathbf{D}_M^z \end{bmatrix}^T \boldsymbol{\delta}_{i'j'k'}^{p} \quad (5)$$

$$\mathbf{D}_M = [\mathbf{D}_M^x, \mathbf{D}_M^y, \mathbf{D}_M^z]^T$$

where $\mu_{i'j'k' \rightarrow ijk}^{p}$ is the contribution of the neighboring cell $\mathbb{C}_{i'j'k'}$ to the cell $\mathbb{C}_{ijk}$ ($L_{i'j'k'}^{\mu} < L_{ijk}^{\mu}$). The cell's μ_{ijk}^{p} is assigned as the average neighbor contribution ($\mu_{i'j'k' \rightarrow ijk}^{p}$) weighted by the neighbor's $\sigma_{i'j'k'}^{p}$. The cell's σ_{ijk}^{p} is assigned as the average of the neighbors' $\sigma_{i'j'k'}^{p}$.

Algorithm 3 Mean Propagation
Given derived mean propagation ordering, $\mathbb{O}^{\mu}$

1: **for** $\mathbb{C}_{ijk} \in \mathbb{O}^{\mu}$ **do**
2:     **if** $L_{ijk}^{\mu} = 0$ **then**
3:        $\mu_{ijk}^{p}, \sigma_{ijk}^{p} = \mu_{ijk}^{m}, \sigma_{ijk}^{m}$
4:     **else**
5:        $Contributions \leftarrow \varnothing$ ▷ (Empty Set)
6:        $Weights \leftarrow \varnothing$
7:        **for** $\mathbb{C}_{i'j'k'} \in Neighbors(\mathbb{C}_{ijk})$ **do**
8:           **if** $L_{i'j'k'}^{\mu} < L_{ijk}^{\mu}$ **then**
9:              Calculate $\mu_{i'j'k' \rightarrow ijk}^{p}$ by Eq. (5)
10:              Add $\mu_{i'j'k' \rightarrow ijk}^{p}$ to $Contributions$
11:              Add $\sigma_{i'j'k'}^{p}$ to $Weights$
12:           **end if**
13:        **end for**
14:        $\mu_{ijk}^{p} \leftarrow WeightedAverage(Contributions, Weights)$
15:        $\sigma_{ijk}^{p} \leftarrow Average(Weights)$
16:     **end if**
17: **end for**

C. Curiosity Derivation and Path Planning

In order to support the field estimation process with informative data and especially achieve rapid radiation field mapping, a planning method is further proposed. Towards determining the next-most-informative radiation waypoint, the method calculates a curiosity metric for each cell in $\mathbb{M}$. This metric balances an exploration-exploitation behavior, maintaining high curiosity in areas in which little information has been obtained and for which a high radiation mean has been propagated, while remaining curious about completely unknown areas of $\mathbb{M}$. An overall metric of each cell's curiosity, ρ_{ijk}, is found by Eq. (6), where $\|\mathbf{H}_{ijk}^{p}\|$ denotes the norm of the propagated gradient entropy, and H^f is a parameterized entropy scale factor. As the norm of the propagated entropy approaches the entropy scale factor, the cell's curiosity approaches 0, thus directing the robot away from well sampled cells:

$$\rho_{ijk} = \left(1 - \frac{\|\mathbf{H}_{ijk}^p\|}{H^f}\right)\Big|_0^1 \times \mu^p \qquad (6)$$

Given 3D bounds on $\mathbb{M}$ which are safe for robot traversal, the method finds the grid cell with the largest ρ_{ijk} within those bounds. This next-best-informative waypoint is selected and the method plans a path ending at this point. The path is supplemented with intermediate waypoints between the current position and the target position by discretizing the path at a regular, parameterized interval. The intermediate waypoints are displaced by random displacement vectors sampled from a uniform distribution to provide greater variance in the position of readings throughout the path, thus improving the quality of the derived gradients along the path.

V. RMF-γ RADIATION MAPPING ROBOT

This section provides an overview of the design of the Resilient Micro Flyer-γ (RMF-γ), alongside its navigation, radiation sensing, and processing solution.

A. Resilient Micro Flyer Airframe

The design of RMF-γ focuses on collision-tolerance and is depicted in Figure 2. The main component of the collision-tolerant frame is fabricated using carbon-balsa sandwich material (total width equal to 6.35mm with 1mm carbon on each side) leading to a total airframe weight of 96g. The frame design of RMF-γ is tailored to keeping the weight low, and ensuring collision-tolerance especially against lateral impacts. In terms of propulsion, RMF-γ integrates four T-Motor F1507 3800KV DC brushless motors. Finally, the robot integrates a PixRacer R15 as its low-level autopilot unit offering attitude and thrust control. High-level position control and autonomous navigation is facilitated through a distinct ARM-based multi-core processing board as detailed further in this section. The total weight of RMF-γ, including all components and its battery is 540g.
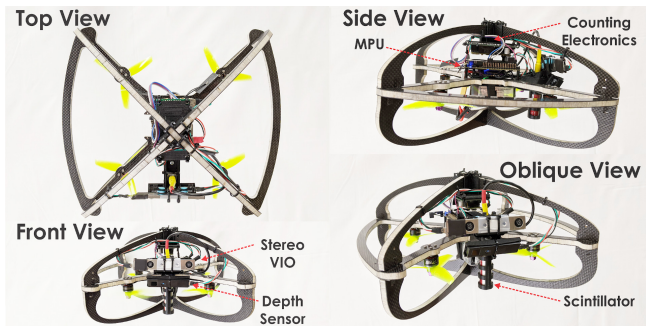

Fig. 2. RMF-γ top, side, front, and oblique views.

B. Radiation Sensing

RMF-γ integrates an Scionix V10B10 Thallium-doped Cesium Iodide (CsI(Tl)) scintillator combined with a Silicon Photomultiplier (SiPm). The detector is interfaced using custom–designed pulse counting and spectroscopy circuitry weighing 18g. Calibration details of the sensor are presented in [21]. The scintillator is interfaced by custom-built counting electronics using an ARM microprocessor. The counting circuitry counts voltage pulses from the SiPm, and reports the readings at a rate of 10Hz to the high level processor, which maintains a sliding window average, using a window size of 10, in order to report measurements to the mapping framework in CPS.

C. Navigation Sensing and Processing Payload

The navigation sensing payload of RMF-γ is tailored to the goal of robust autonomy, while maintaining a lightweight configuration. In particular, RMF-γ integrates a Realsense T265 tracker delivering visual-inertial odometry. Simultaneously, in order to acquire more accurate reconstructed maps, a PMD Picoflexx Time-Of-Flight 3D camera with horizontal and vertical Field-of-View $[F_H, F_V] = [60, 45]°$ and range up to 5m was integrated. The above are processed by the integrated Main Processing Unit (MPU) relying on the Khadas VIM3 offering 4 A311D Cortex-A73 cores at 2.2GHz paired with 2 Cortex-A53 cores at 1.8GHz and 4GB of LPDDR4X RAM. This board is responsible for all computational tasks onboard.

VI. EVALUATION STUDIES

To evaluate the performance of the autonomous distributed radiation mapping method, this section presents the results of two experiments using the RMF-γ platform and three actual gamma radiation sources. The gamma radiation sources used consist of mine tailings contained in buckets collected from an abandoned uranium mine located near Reno, Nevada. In both of the presented experiments, two of the sources are placed in a stacked configuration just outside the safe flight bounds for RMF γ, while the third source is placed 4.37m away within the safe flight bounds.

In the first experiment, the robot executes the radiation curiosity path given by the distributed radiation mapping algorithm. The plots on the left of Figure 3 show four instances of the experiment, depicting RMF-γ's path in pink, the derived propagated gradients with red arrows, and the propagated mean intensity field in the background of the plot. The 3D plot on the right of Figure 3 shows the final propagated field with the gradient arrows colored by their respective cell's propagated mean, the robot trajectory in pink, and the propagated mean at 0.25m as a height-map. All plots depict the true location of the radiation sources as green cylinders within the height-map.

Figure 4 shows four instances of the second experiment, in which the robot is guided by a fixed-grid lawnmower trajectory, whose waypoints are separated by 1m, 0.65m, 1m on the x, y, z axes respectively. In both experiments, the radiation field estimation method reconstructs a faithful representation of the nuclear radiation field as per first-principle modeling would allow us to predict. Certain differences however exist between the two experiments.

The most important distinction highlighted by the two studies shows how the derived curiosity waypoints quickly find the radiation source and iteratively refine the radiation intensity estimate, while also covering the entire space. In
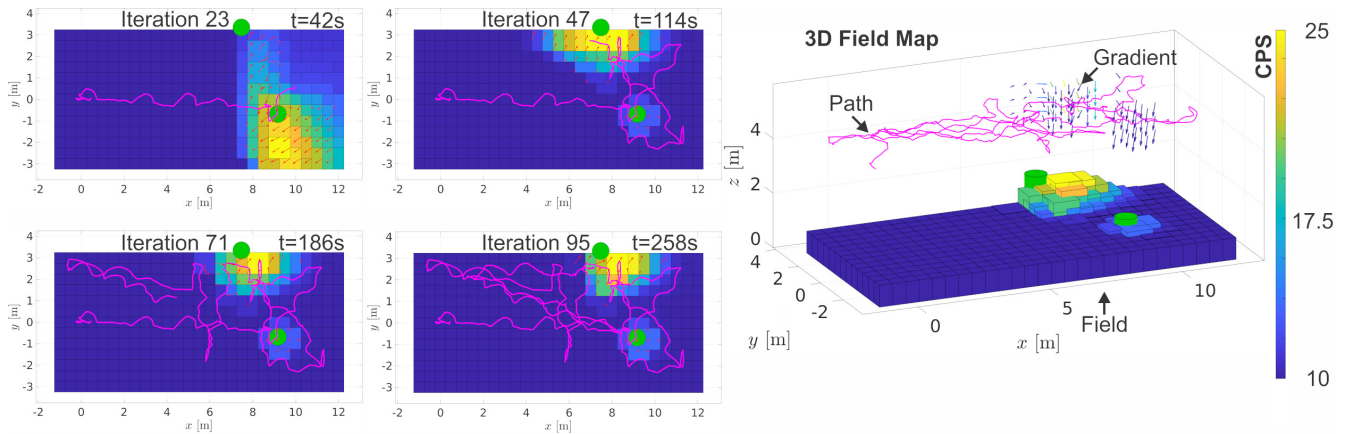
Fig. 3. Curiosity-Driven 3D Radiation Field Mapping with RMF-γ. The 4 plots on the left depict iterations of the mapping experiment showing the progression of the propagated radiation field throughout the experiment. The robot trajectory is shown in pink, the propagated radiation field gradients are shown by red arrows, and the background is colored by the propagated mean, measured in Counts Per Second (CPS), found at a height of 0.25m. The plot on the right shows the final estimated radiation field, highlighting the 3D nature of the field estimation method, depicting the robot trajectory in pink, the propagated radiation gradients colored by their cell's propagated mean, as well as a height-map depicting the propagated mean intensity at a height of 0.25m. The true positions of the radiation sources are depicted by green cylinders and the path and gradients are translated up the z axis for visualization purposes.
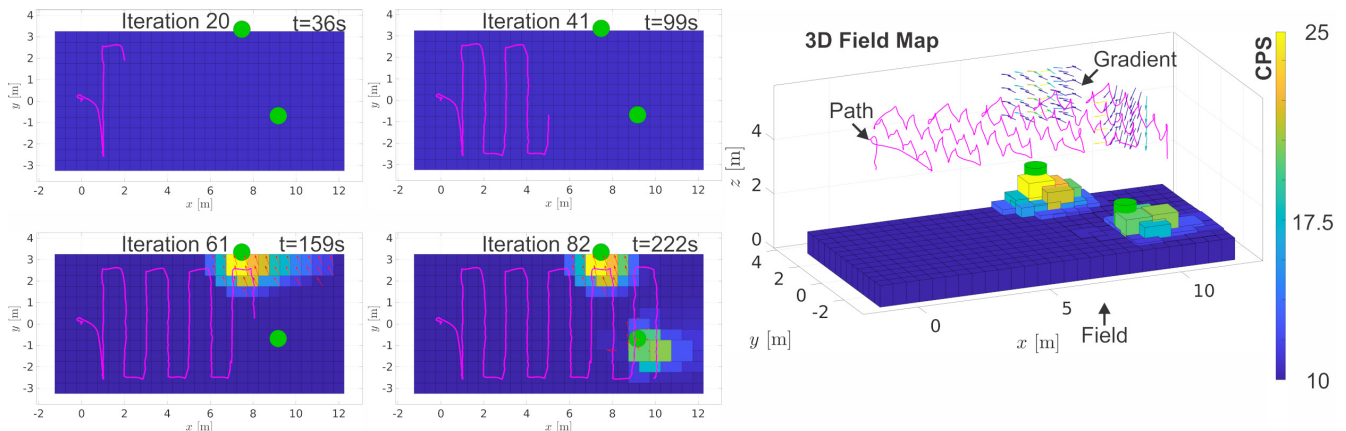

Fig. 4. Fixed Waypoint Grid 3D Radiation Field Mapping with RMF-γ. The 4 plots on the left depict iterations of the mapping experiment showing the progression of the propagated radiation field. The robot trajectory is shown in pink, the propagated radiation field gradients are shown by red arrows, and the background is colored by the propagated mean, measured in Counts Per Second (CPS), found at a height of 0.25m. The plot on the right shows the final estimated radiation field, depicting the robot trajectory in pink, the propagated radiation gradients colored by their cell's propagated mean, as well as a height-map depicting the propagated mean intensity at a height of 0.25m. The true positions of the radiation sources are depicted by green cylinders and the path and gradients are translated up the z axis for visualization purposes.

the curiosity experiment, iteration 47 is reached after 114 seconds, while in the lawnmower experiment, iteration 61 is reached after 159 seconds, showing that the curiosity planner provides a rapid estimate of the field in a shorter amount of time. This difference is further exaggerated in larger environments where the endurance necessary to map the radiation fields with a fixed-grid trajectory would be significantly greater than the platform's endurance. At the same time, if a mission only has to address the mapping of a small enough environment, then a dense and carefully selected fixed pattern provides high-quality spatial distribution of the measurements and thus predicted field accuracy.

Finally, this experiment highlights the importance of 3D distributed radiation field estimation. Visible from both Figures 3 and 4 is the intensity value of the field, alongside the predicted gradients. Given an aerial robot capable of measuring the field at a range of z-heights above the dis-

tributed field and subject to the inverse-square law property of radiation propagation, it would be challenging for a 2D or 2.5D method to correctly estimate mean intensities given measurements close to, as well as far above the source.

VII. CONCLUSIONS

In this work, a new method for autonomous distributed 3D nuclear radiation field mapping was proposed and experimentally verified based on a custom-designed resilient micro flyer. The algorithm uses sequentially-acquired radiation readings to reconstruct an accurate estimate of the radiation field. To achieve this goal it estimates the field mean and gradient, while it further allows automatic guidance of a robot in order to iteratively acquire informative scintillator readings. A set of experiments is presented and serves to verify the quality of the estimated map and the benefits of curiosity-driven path planning in time-constrained missions.

REFERENCES

[1] World Nuclear Association, "Nuclear Power in the World Today." [Online]. Available: http://www.world-nuclear.org

[2] K. D. Jarman, E. A. Miller, R. S. Wittman, and C. J. Gesh, "Bayesian radiation source localization," *Nuclear technology*, vol. 175, no. 1, pp. 326–334, 2011.

[3] H. Wan, T. Zhang, and Y. Zhu, "Detection and localization of hidden radioactive sources with spatial statistical method," *Annals of Operations Research*, vol. 192, no. 1, pp. 87–104, 2012.

[4] H. E. Baidoo-Williams, "Maximum likelihood localization of radiation sources with unknown source intensity," *arXiv preprint arXiv:1608.00427*, 2016.

[5] H. E. Baidoo-Williams, R. Mudumbai, E. Bai, and S. Dasgupta, "Some theoretical limits on nuclear source localization and tracking," in *Information Theory and Applications Workshop (ITA), 2015*. IEEE, 2015, pp. 270–274.

[6] G. Cordone, R. R. Brooks, S. Sen, N. S. Rao, C. Q. Wu, M. L. Berry, and K. M. Grieme, "Improved multi-resolution method for mle-based localization of radiation sources," in *Information Fusion (Fusion), 2017 20th International Conference on*. IEEE, 2017, pp. 1–8.

[7] S. Martínez, "Distributed interpolation schemes for field estimation by mobile sensor networks," *IEEE Transactions on Control Systems Technology*, vol. 18, no. 2, pp. 491–500, 2010.

[8] Y. Wang and P. Ishwar, "Distributed field estimation with randomly deployed, noisy, binary sensors," *IEEE Transactions on Signal Processing*, vol. 57, no. 3, pp. 1177–1189, 2009.

[9] H. M. La and W. Sheng, "Distributed sensor fusion for scalar field mapping using mobile sensor networks," *IEEE Transactions on cybernetics*, vol. 43, no. 2, pp. 766–778, 2013.

[10] C. Zhang, D. Arnold, N. Ghods, A. Siranosian, and M. Krstic, "Source seeking with non-holonomic unicycle without position measurement and with tuning of forward velocity," *Systems & control letters*, vol. 56, no. 3, pp. 245–252, 2007.

[11] S. Pang and J. A. Farrell, "Chemical plume source localization," *IEEE Transactions on Systems, Man, and Cybernetics, Part B (Cybernetics)*, vol. 36, no. 5, pp. 1068–1080, 2006.

[12] C. G. Mayhew, R. G. Sanfelice, and A. R. Teel, "Robust source-seeking hybrid controllers for autonomous vehicles," in *American Control Conference, 2007. ACC'07*. IEEE, 2007, pp. 1185–1190.

[13] R. A. Cortez, H. G. Tanner, and R. Lumia, "Distributed robotic radiation mapping," in *Experimental Robotics*. Springer, 2009, pp. 147–156.

[14] A. A. R. Newaz, S. Jeong, H. Lee, H. Ryu, N. Y. Chong, and M. T. Mason, "Fast radiation mapping and multiple source localization using topographic contour map and incremental density estimation," in *Robotics and Automation (ICRA), 2016 IEEE International Conference on*. IEEE, 2016, pp. 1515–1521.

[15] G. Christie, A. Shoemaker, K. Kochersberger, P. Tokekar, L. McLean, and A. Leonessa, "Radiation search operations using scene understanding with autonomous uav and ugv," *Journal of Field Robotics*, 2016.

[16] K. Vetter, D. Chivers, and B. Quiter, "Advanced concepts in multi-dimensional radiation detection and imaging," in *Nuclear Threats and Security Challenges*. Springer, 2015, pp. 179–192.

[17] A. A. R. Newaz, S. Jeong, H. Lee, H. Ryu, and N. Y. Chong, "Uav-based multiple source localization and contour mapping of radiation fields," *Robotics and Autonomous Systems*, vol. 85, pp. 12–25, 2016.

[18] J. Towler, B. Krawiec, and K. Kochersberger, "Radiation mapping in post-disaster environments using an autonomous helicopter," *Remote Sensing*, vol. 4, no. 7, pp. 1995–2015, 2012.

[19] M. Maimone, L. Matthies, J. Osborn, E. Rollins, J. Teza, and S. Thayer, "A photo-realistic 3-d mapping system for extreme nuclear environments: Chernobyl," in *Intelligent Robots and Systems, 1998. Proceedings., 1998 IEEE/RSJ International Conference on*, vol. 3. IEEE, 1998, pp. 1521–1527.

[20] E. Rolf, D. Fridovich-Keil, M. Simchowitz, B. Recht, and C. Tomlin, "A successive-elimination approach to adaptive robotic source seeking," *IEEE Transactions on Robotics*, 2020.

[21] F. Mascarich, T. Wilson, C. Papachristos, and K. Alexis, "Radiation source localization in gps-denied environments using aerial robots," in *IEEE International Conference on Robotics and Automation (ICRA)*, May 2018.

[22] F. Mascarich, C. Papachristos, T. Wilson, and K. Alexis, "Distributed radiation field estimation and informative path planning for nuclear environment characterization," in *2019 International Conference on Robotics and Automation (ICRA)*. IEEE, 2019, pp. 2318–2324.